

Defect Structure of Ultrathin Ceria Films on Pt(111): Atomic Views from Scanning Tunnelling Microscopy[†]

David C. Grinter,^{*,§} Roslinda Ithnin,^{*,§,⊥} Chi L. Pang,^{*,§} and Geoff Thornton^{*,§,§}

London Centre for Nanotechnology, University College London, London WC1H 0AJ, U.K., Department of Chemistry, University College London, London, WC1H 0AJ, U.K., and Pusat Asasi Sains, Universiti Malaya, 50603 Kuala Lumpur, Malaysia

Received: March 31, 2010

Atomically resolved scanning tunnelling microscopy (STM) images have been obtained on ultrathin films of CeO₂(111) supported on Pt(111). The ultrathin films were grown in two ways, by reactive deposition in an oxygen atmosphere and by postoxidation of Ce/Pt surface alloys. STM results are compared with previously reported high-temperature STM and noncontact atomic force microscopy (NC-AFM) images of the native CeO₂(111) surface. The similarity between these images is striking and allows a number of defects and adsorbates in our ultrathin film to be assigned. Moreover, the similarity in structure between the native oxide and the ceria ultrathin film indicates that it is an excellent topographic mimic of the native oxide.

1. Introduction

The study of ceria (CeO₂) is currently of great interest, with proven technological applications arising from its wide-ranging catalytic properties. For instance, it is used in exhaust gas purification in automotive catalytic converters and in the water–gas shift reaction to produce H₂.^{1,2} The key to these properties lies in the high mobility of lattice oxygen leading to excellent oxygen storage and release, as well as the promotion of noble metal activity.³ Both aspects are thought to be determined by the nature, concentration, and mobility of lattice defects, especially oxygen vacancies. It is well-known that the defect structure of transition-metal oxide surfaces is key to their reactive behavior. For rare-earth oxides such as ceria, there is the added complication that the removal of neutral oxygen to form a vacancy leaves electrons localized on previously empty f states.⁴ There is the resultant effect for ceria that the reduction of Ce⁴⁺ to Ce³⁺ occurs for two cations per oxygen vacancy, leading to efficient reversible oxygen release and hence a high activity for a number of catalytic systems.^{2,5} A further potentially important role of vacancies is in the binding of catalytically active metals such as Au, recently discovered to be a highly active catalyst for the water–gas shift reaction.^{6–8}

Since its inception in the late 1980s, scanning probe microscopy (particularly scanning tunnelling microscopy, STM) has become a hugely important tool for directly investigating the defective nature of surfaces since the technique allows individual point defects to be probed. A key limitation to the implementation of STM in the study of ceria is the insulating nature of the native oxide. Stoichiometric CeO₂ has a band gap of about 6 eV, and as a result, the use of STM has been limited mainly to high-temperature (>575 K) studies.^{9,10} The complementary technique of noncontact atomic force microscopy (NC-AFM) has also been used to study the surface structure of CeO₂(111) at room and cryogenic temperatures. This has

provided important insights, especially with regards to adsorbate–surface interactions not seen at the elevated temperatures required for single-crystal STM.^{11–14}

One means of studying insulating metal oxides using charged particle techniques is to prepare ultrathin films on conducting substrates.¹⁵ A number of metal supports have proved successful in this regard, including Ru(0001),^{16,17} Pd(111),¹⁸ Rh(111),^{19,20} Ni(111),¹⁷ Re(0001),²¹ Cu(111),^{22,23} and Pt(111),^{24,25} with STM having been employed in some of these cases.^{16,19,20,23–25}

In this study, we prepare ultrathin ceria films on a Pt(111) substrate. Our images suggest that ultrathin films grown in this way mimic the native surface very closely in terms of the structural elements present. In particular, a number of point defects and arrays of such defects previously observed in STM and NC-AFM of the native surfaces can be identified in the ultrathin films produced here.

2. Experimental Details

All STM images presented here were recorded in the constant current mode using a commercial room-temperature AFM/STM (Omicron GmbH) housed in an ultrahigh vacuum (UHV) analysis chamber with a base pressure of 1×10^{-10} mbar. STM tips were prepared by electrochemical etching of W wire (Advent) in 2 M NaOH, followed by degassing at ~500 K in UHV and Ar sputtering. Voltage pulses and high bias scans (negative and positive) were performed during routine STM operation in order to condition the tip apex to allow stable tunnelling with atomic resolution imaging.

Samples were prepared in a preparation chamber with a base pressure of 1×10^{-10} mbar attached to the analysis chamber. The Pt(111) crystal was prepared by cycles of Ar⁺ sputtering (1.5 keV) and annealing at 1100 K in UHV until a well-ordered Pt(111) pattern was observed in low-energy electron diffraction (LEED) and impurities were below the detection limit of Auger electron spectroscopy (AES). In order to remove minor carbon contamination, cycles of annealing at 1100 K in 1×10^{-6} mbar of O₂ were also occasionally performed. Preparation of ceria films employed two methods, (1) postoxidizing a Ce/Pt alloy

[†] Part of the “D. Wayne Goodman Festschrift”.

* To whom correspondence should be addressed. Tel.: (+44) 207 679 7979. Fax: (+44) 207 679 7463. E-mail: g.thornton@ucl.ac.uk.

[§] London Centre for Nanotechnology, University College London.

[§] Department of Chemistry, University College London.

[⊥] Universiti Malaya.

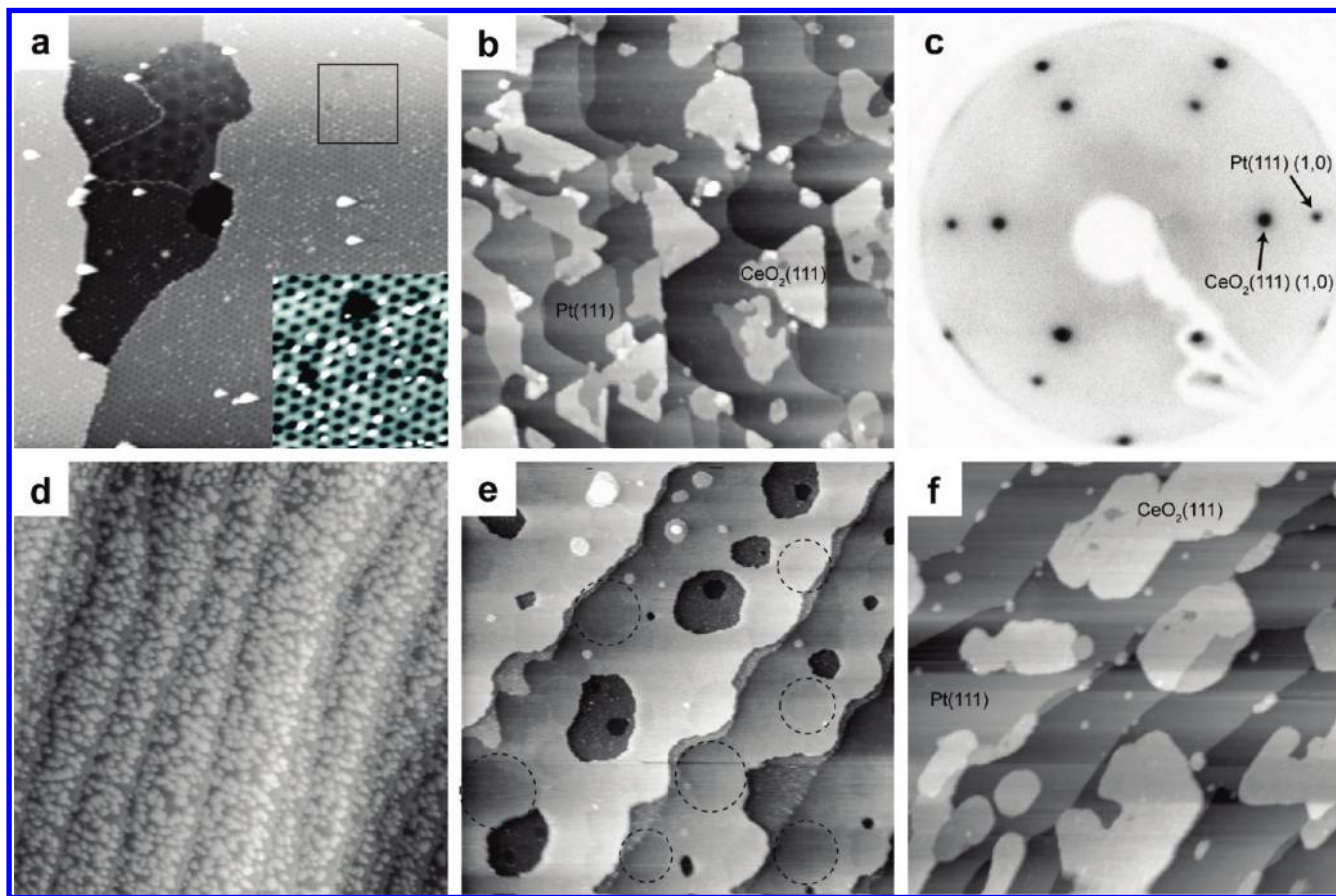


Figure 1. Large-area STM and LEED results contrasting the two methods for formation of CeO₂(111) ultrathin films on Pt(111), via surface alloys (a–c) and reactive deposition (d–f). (a) STM image ($200 \times 200 \text{ nm}^2$, $V_s = 1.76 \text{ V}$, $I_t = 0.23 \text{ nA}$) of the Pt/Ce surface alloy phases formed by PVD of $\sim 0.5 \text{ ML}$ of Ce and UHV annealing at 1020 K. The fine structure of the alloy area that is bounded by a black square is shown expanded in the inset ($25 \text{ nm} \times 25 \text{ nm}$). (b) STM image ($200 \times 200 \text{ nm}^2$, $V_s = -3.00 \text{ V}$, $I_t = 0.10 \text{ nA}$) of a 0.5 ML ceria film after oxidation of (a) at 1000 K in $5 \times 10^{-6} \text{ mbar}$ of O₂. Atomically flat terraces and single atomic steps on bare Pt(111) are observed along with islands of CeO₂(111) with heights corresponding to one or two O–Ce–O trilayers. (c) LEED ($E_p = 67.5 \text{ eV}$) of ceria film (b) displaying Pt(111) (1×1) and CeO₂(111) (1.37×1.37) relative to Pt(111). (d) STM image ($200 \times 200 \text{ nm}^2$, $V_s = 2.00 \text{ V}$, $I_t = 0.25 \text{ nA}$) of small ceria particles after reactive deposition of cerium in $1 \times 10^{-6} \text{ mbar}$ of O₂. (e) STM image ($200 \times 200 \text{ nm}^2$, $V_s = -3.20 \text{ V}$, $I_t = 0.20 \text{ nA}$) of a 0.8 ML ceria film after postoxidation of (d) at 850 K in $1 \times 10^{-6} \text{ mbar}$ of O₂. The ultrathin ceria film of one trilayer thickness (0.3 nm) covers $\sim 80\%$ of the surface; examples of the area examined at atomic resolution in Figure 2 are highlighted by dashed circles. A few holes in the ceria are observed, revealing the Pt substrate and/or some partially formed oxide. (f) STM image ($200 \times 200 \text{ nm}^2$, $V_s = -3.20 \text{ V}$, $I_t = 0.20 \text{ nA}$) of a 0.8 ML ceria film after oxidation of (d) at 920 K in $5 \times 10^{-6} \text{ mbar}$ of O₂. Regions of bare Pt(111) are observed with isolated CeO₂(111) islands with thicknesses of one or two trilayers, as for film (b).

as described by Berner and Schierbaum²⁴ and (2) by reactive deposition in O₂, as described for ceria films grown on Rh(111).¹⁶

For the postoxidized film, cerium metal (Alfa Aesar, 99.9%) was evaporated onto the clean Pt(111) substrate at 300 K via physical vapor deposition (PVD) from an electron beam evaporator and then annealed in UHV at 1020 K for 3 min. Further annealing to 1000 K in an O₂ pressure of $5 \times 10^{-6} \text{ mbar}$ for 7 min led to a CeO₂(111) ultrathin film with a (1.37×1.37) LEED pattern relative to Pt(111). In the reactive deposition procedure, the Pt substrate was held at $\sim 600 \text{ K}$, with the cerium metal evaporated from the same doser in $1 \times 10^{-6} \text{ mbar}$ of O₂. This partially formed oxide film was then annealed to 850 K in $1 \times 10^{-6} \text{ mbar}$ of O₂ for a few minutes followed by short heating cycles at 920 K in $5 \times 10^{-6} \text{ mbar}$ of O₂. Temperatures were monitored with an optical pyrometer (Minohta).

Due to the O–Ce–O trilayer structure parallel to fluorite-type CeO₂(111), we define a monolayer (ML) as one trilayer unit with a thickness of 0.31 nm. All coverages were estimated from the film thickness, and the surface area fraction was measured by STM.

3. Results and Discussion

STM analysis shows that the clean Pt(111) substrates that we prepare consist mainly of flat terraces a few hundred nm wide, separated by monatomic steps of height 0.23 nm. Atomically resolved images of the clean surface display a nonreconstructed (1×1) hexagonal arrangement of features consistent with LEED and indicate a distance between features of 0.28 nm, as expected on the basis of previous work and consistent with the interatomic spacing of Pt(111), which is 0.2775 nm. As described in the experimental section, postoxidized films are grown via an intermediate Pt/Ce surface alloy such as that displayed in Figure 1a. These alloy phases can be identified in LEED by the presence of (2×2) and (2×2)R30° reflexes and in STM by their characteristic moiré patterns.^{26,27}

Postoxidation of these alloys leads to the formation of thin films of ceria, a typical STM image being displayed in Figure 1b alongside the corresponding LEED pattern (Figure 1c). The STM image shows that the film (estimated from STM to have a coverage of $\sim 0.5 \text{ ML}$) consists of isolated islands with geometric shapes (hexagonal and triangular) of lateral dimension 30–50 nm. The apparent thickness of these islands is 0.3 or

0.6 nm, consistent with one or two O–Ce–O trilayers, respectively. This trilayer stacking implies that the film is oxygen-terminated CeO₂(111), the thermodynamically most stable surface and that which may form the major fraction of active catalyst surface.^{24,28}

Figure 1d–f shows STM images taken from ceria films grown by reactive deposition. A STM image taken after Ce dosing in an O₂ pressure of 1×10^{-6} mbar (Figure 1d) shows a nearly complete coverage of the Pt surface by small (~ 10 nm diameter) particles of ceria. These particles are uniformly distributed over the surface, with no preference for step edges. Upon annealing at 850 K in 1×10^{-6} mbar of O₂ for 5 min, a near-complete film is formed, as shown in Figure 1e. This large-area STM image shows the presence of a ceria film across the Pt substrate covering about 80% of the surface. Individual steps on this film have a height of 0.3 nm, consistent with a single trilayer of CeO₂. There are a number of holes within the terraces. Although atomic resolution imaging was not possible within these holes, their appearance in STM is visibly different from that of the ceria, and their depth is approximately one trilayer. As such, we assume that these holes correspond either to the underlying Pt or a region of partially formed oxide. A number of other bright features with geometric shapes and lateral sizes of a few nm are visible on the terraces and are likely the start of the formation of a second ceria trilayer. Upon annealing the film in Figure 1e to 920 K in 5×10^{-6} mbar of O₂ for 4 min, the structure of the ceria film is changed dramatically, as displayed in Figure 1f. The ceria coalesces to form isolated islands with a layered structure consistent with one or two trilayers of CeO₂. These islands are similar in appearance to those formed via the postoxidation route in Figure 1b, although they display less angular shapes, tending more toward hexagonal shapes.

Although we are unable to monitor the oxidation state of the ceria within these films in situ, examination of the STM images allows a number of conclusions to be drawn. A minority area of the terraces seen in Figure 1e displays a noticeably different contrast in STM (some of these areas are highlighted by dashed circles); an atomically resolved image of such an area is shown in Figure 2. Figure 2a shows the edge of one of these minority areas, inside of which a characteristic hexagonal motif is observed. This motif is very similar to that assigned to Ce₂O₃ by Berner and Schierbaum,²⁴ and we make the same assignment here. It is important to note that although the structure that we image is similar, the Ce₂O₃ phase was formed in a different way. In the previous study, Ce₂O₃ was only seen after the majority CeO₂ ultrathin film was annealed for 10 min at 1000 K in UHV.²⁴

The image in Figure 2b is of the same area and was taken at a quite different bias voltage of -0.22 V. Hexagonal lattices can be seen in both the minority Ce₂O₃ phase as well as the majority ceria phase. The unit cells of these are rotated by 15° with respect to each other, and there is additional fine structure seen in the Ce₂O₃ phase to that reported by Berner and Schierbaum.²⁴ This bias voltage is much less negative than that normally required for atomic resolution imaging of filled states on CeO₂(111), which is typically -3.2 V. The latter value is thought to arise from tunnelling from O 2p orbitals. The less negative value of -0.22 V indicates a different origin, possibly involving substrate electronic states.

The ratio of lattice spacings of Pt(111)/CeO₂(111) from the LEED patterns of the ceria films is measured at 1:1.37 (± 0.01), a deviation from the ideal ratio of the respective single crystals of 1:1.40.²⁹ This discrepancy may arise from the large lattice mismatch between the support and film, which gives rise to a

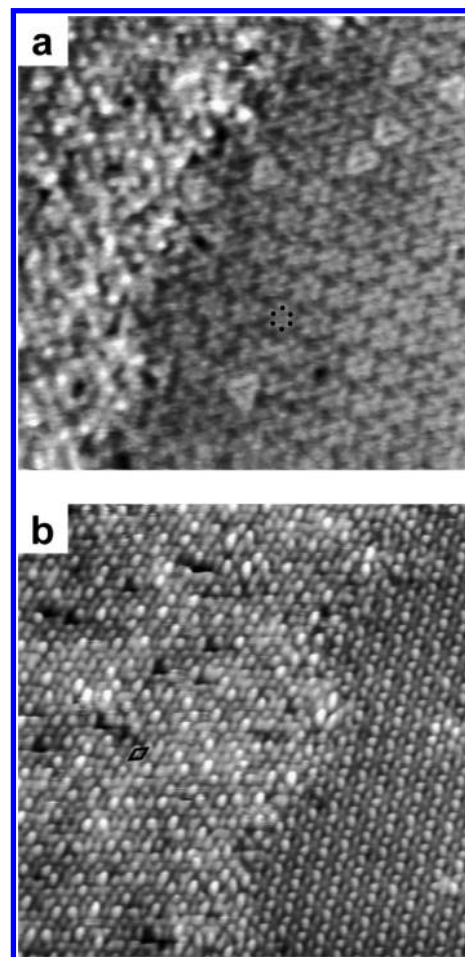


Figure 2. Atomically resolved STM images (15×15 nm², $I_t = 0.20$ nA) at different sample biases of a region of the ceria thin film displayed in Figure 1e as highlighted by dashed circles at different sample biases, (a) $V_s = -3.20$ V and (b) $V_s = -0.22$ V.

strain-induced contraction of the ceria ultrathin film lattice relative to the single crystal. This may have an important effect regarding the defect structure present in the film, as suggested by Castellarin et al.³⁰ who report strain-induced ordering of oxygen vacancies at the surface of a similar CeO₂(111) film.

Atomic Resolution Imaging of Defects and Adsorbates.

An understanding of the interaction of adsorbate molecules with CeO₂(111), particularly with regards to surface defects, may be key to gaining insight into the mechanism of ceria catalysis. The next section of results focuses on atomically resolved imaging of the ultrathin films. In all images presented here, the sample is held at negative bias relative to the tip during scanning so that filled sample states are imaged. As such, the bright spots in all of the atomically resolved images are assigned to oxygen atoms due to the dominant tunnelling contributions from O 2p orbitals at the high biases used for best contrast.⁹ Measurement of the interatomic spacing between these bright spots yields a value of 0.38 ± 0.03 nm, consistent with the ideal parameters for both CeO₂(111) (0.3826 nm) and Ce₂O₃(0001) (0.3888 nm)²⁴ and agreeing with our measured LEED ratio of 1:1.37 with respect to the Pt(111) substrate. Imaging of the empty states with atomic resolution is also possible (not shown), in which case it is assumed that the Ce⁴⁺ cations provide most of the empty states for image formation and as such appear as bright protrusions in STM. As oxygen vacancies are thought to be critical in determining the catalytic properties of ceria, we have chosen to use filled state imaging so that surface oxygen

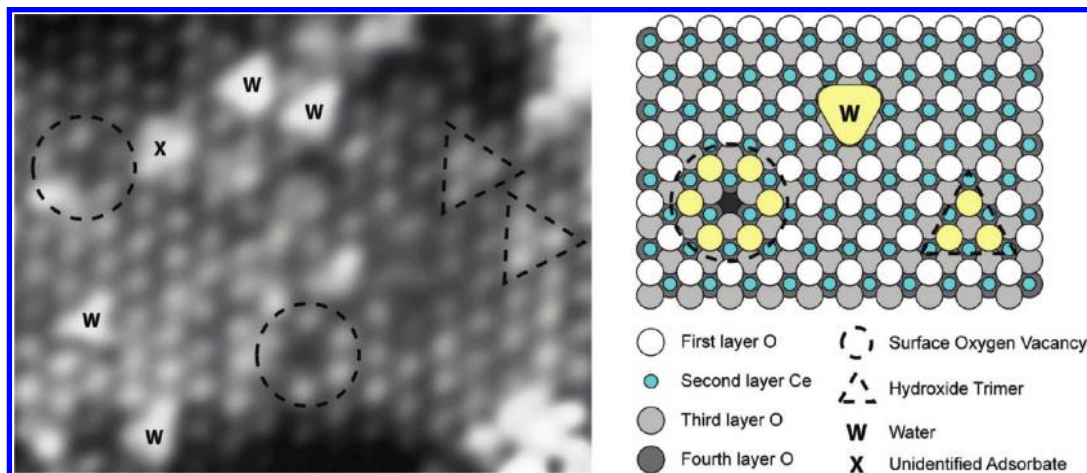


Figure 3. Atomically resolved, filled state, STM image ($5 \times 4 \text{ nm}^2$, $V_s = -3.20 \text{ V}$, $I_t = 0.20 \text{ nA}$), and structural model of vacancies and adsorbates on an ultrathin film of $\text{CeO}_2(111)$ on $\text{Pt}(111)$. Bright spots correspond to top-layer oxygen termination of the surface, with identification of adsorbed water, hydroxide trimers, and surface oxygen vacancies possible by comparison with NC-AFM^{12,14} and high-temperature STM.⁹ The assignments are highlighted in the structural model. Water molecules are observed exclusively above second-layer Ce atoms.

vacancies should appear simply as dark spots. Such filled state imaging also facilitates comparison with NC-AFM images, which also show surface oxygen atoms as bright features.^{11–14}

Figure 3 is an atomically resolved STM image recorded from a 0.9 nm thick $\text{CeO}_2(111)$ film (three trilayers) grown by postoxidation. The image displays a number of characteristic features. The dashed circles are drawn around depressions that are surrounded by six slight protrusions. By comparison with high-temperature STM images by Esch et al.⁹ and 80 K NC-AFM images by Torbrugge et al.¹⁴ taken from single-crystal $\text{CeO}_2(111)$, we assign these depressions to surface oxygen vacancies and the surrounding protrusions to oxygen atoms. The magnitude of the outward relaxation of the surrounding O atoms is not as pronounced in our thin film as that observed on the single crystal, and in some cases, no protrusion is observed at all.

A number of bright triangular features (marked **W** in Figure 3) are seen across the surface of the film and are centered at three-fold hollow positions between three top-layer oxygen sites. From room-temperature NC-AFM studies of single-crystal $\text{CeO}_2(111)$,¹² water has been shown to adsorb solely in these same three-fold hollow sites, as illustrated in the model of Figure 3. Thus, by comparison with the NC-AFM images, we can assign these triangular features to adsorbed water molecules, the source of water being the residual vacuum. Such adsorbed water has not previously been seen in STM studies of the $\text{CeO}_2(111)$ single-crystal surface, presumably due to the elevated temperatures employed.

Also highlighted in Figure 3 are a number of triangular arrangements of bright spots (marked by dashed triangles), each of which lie atop three adjacent top-layer oxygen ions. The orientation of these triangular features is the opposite to that found for adsorbed water above, indicating that they are centered on the third-layer oxygen sublattice, as illustrated in Figure 3. An analogous feature present in NC-AFM¹² was assigned as triple hydroxide clusters, and we make the same assignment here. A similar feature can also be seen in Figure 3, marked **X**. It is also composed of a triangular protrusion centered on a third-layer oxygen site. However, in this case, the triangle does not resolve into individual spots, suggesting the presence of an as yet unexplained surface feature.

The formation of multiple surface oxygen vacancies has also been observed in our films, for example, in Figure 4, where a

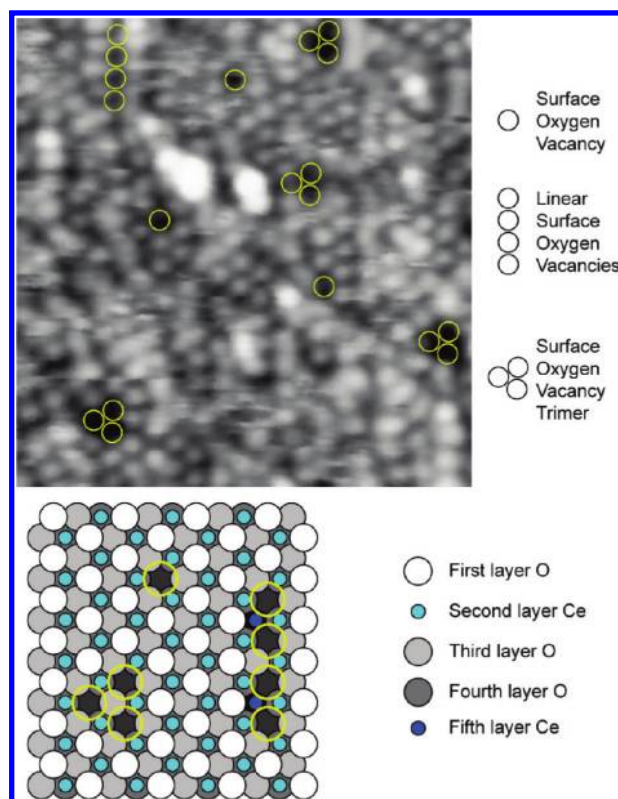


Figure 4. Atomically resolved, filled state, STM image ($6 \times 6 \text{ nm}^2$, $V_s = -3.20 \text{ V}$, $I_t = 0.20 \text{ nA}$), and structural model depicting surface oxygen vacancies on an ultrathin film of $\text{CeO}_2(111)$ on $\text{Pt}(111)$. Bright spots correspond to top-layer oxygen termination of the surface, and surface vacancies are observed as isolated individuals, trimers, and linear arrangements as highlighted by yellow circles superimposed on the STM image. Trimers of surface oxygen vacancies are oriented such that they are centered above a third-layer oxygen site for energetic reasons. The model shows the presence of additional subsurface vacancies in a linear array as proposed by Esch et al.⁹

number of such features are highlighted. The most common multiple vacancy formation seen in our films is that of a trimer of three missing surface oxygen atoms, as seen on single-crystal $\text{CeO}_2(111)$ ^{9,10,12} and also suggested by empty states STM imaging of ultrathin ceria films grown on $\text{Rh}(111)$.³⁰ The vacancy trimers in Figure 4 are all oriented in the same direction, consistent with the observation by Esch et al.⁹ that the only

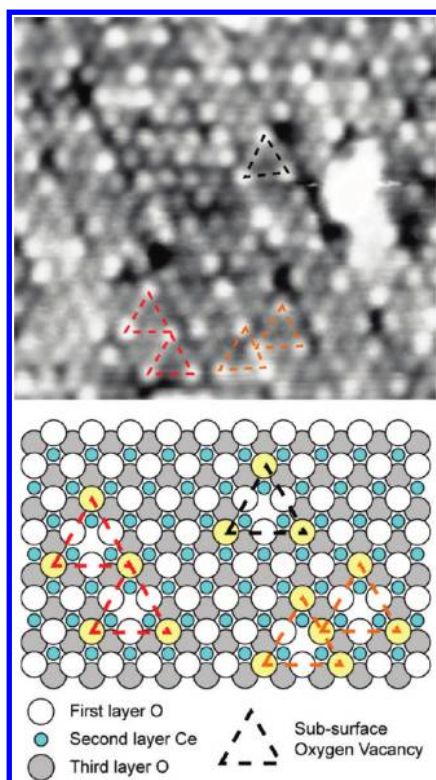


Figure 5. Atomically resolved, filled state, STM image ($7 \times 6 \text{ nm}^2$, $V_s = -3.20 \text{ V}$, $I_t = 0.25 \text{ nA}$), and structural model depicting subsurface oxygen vacancies on a single trilayer ultrathin film of $\text{CeO}_2(111)$ on $\text{Pt}(111)$. Bright spots in the STM correspond to top-layer oxygen termination of the surface, and oxygen vacancies in the third layer result in a characteristic triangular arrangement of protrusions as highlighted by dashed triangles and bright atoms in the structural model. The colored dashed triangles superimposed on the STM image and model highlight common configurations of the subsurface vacancies observed, isolated (black) and adjacent (orange and red).

trimer arrangement seen is that which is centered on a third-layer oxygen site. This arrangement results in just six Ce^{3+} cations in the second layer being exposed rather than an additional Ce^{4+} cation and hence is a more stable arrangement. As well as these trimers, linear surface oxygen vacancies comprising four vacancies can also be observed in Figure 4 and have been seen in many other images not shown here. As seen for the individual surface oxygen vacancies in Figure 3, the protrusion of the surrounding top-layer oxygen atoms around these multiple vacancies is not as prominent on the ceria film compared to the single crystal.

Another common form of defect observed in images of the single-crystal surface is that of a subsurface oxygen vacancy, which appears in STM and NC-AFM as three protrusions of top-layer oxygen sites separated by two lattice spacings in a triangular arrangement and centered above a third-layer oxygen site.^{9,14} We have also observed this type of defect as illustrated in Figure 5, where much of the surface of a ceria film is seen to display this triangular superstructure, indicating a high density of such defects. The image in Figure 5 was taken from a different part of the same film displayed in Figure 1e, formed via the reactive deposition method. A number of arrangements of these subsurface defects are highlighted in Figure 5 by dashed triangles with their vertices centered on the protruding oxygen atoms, demonstrating isolated vacancies (black) and two forms of adjacent vacancies (orange and red). Another characteristic signature of these subsurface vacancies is a small inward relaxation of the other three surface oxygen ions that make up

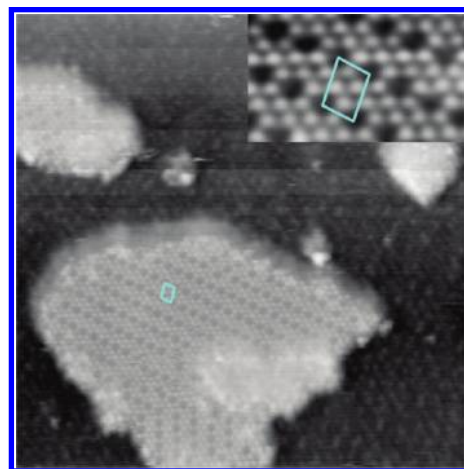


Figure 6. STM image ($25 \times 25 \text{ nm}^2$, $V_s = -3.20 \text{ V}$, $I_t = 0.20 \text{ nA}$) of a heavily reduced ceria thin film formed via reactive deposition. The majority of the surface visible is a single trilayer $\text{CeO}_2(111)$ ultrathin film with a high concentration of subsurface oxygen vacancies (as depicted with atomic resolution in Figure 5). Islands of the next ceria trilayer on top are observed to have linear arrays of ordered surface oxygen vacancies, as shown clearly in the atomically resolved inset $4 \times 2 \text{ nm}^2$ STM image. The unit cell corresponding to these arrays is highlighted in blue and indicates that a quarter of the terminating surface oxygen atoms are missing.

the triangular shape,^{9,14} some evidence of which is present in our images. There are a number of depressions also visible in the STM, likely surface oxygen vacancies, but due to the enhanced contrast of the subsurface vacancies, it is not possible to assign these with a high degree of confidence. Given that this film is only a single trilayer thick, the high density of these subsurface vacancies indicates the highly reduced nature of the film formed by reactive deposition under the preparation conditions used.

As displayed in Figure 1e, there are a number of island structures on top of these films which can be imaged with atomic resolution, as shown in Figure 6. These islands, which are the start of a second ceria trilayer, display an interesting structure, not previously observed, that contrasts with that of the surrounding film which is similar in appearance to the area highlighted in Figure 5. On top of the islands, we observe the terminating oxygen layer with ordered single surface oxygen vacancies. This is highlighted in the inset image in Figure 6, and the array of defects is assigned in matrix notation as

$$\text{CeO}_2\{111\} - \begin{bmatrix} 2 & 1 \\ -1 & 2 \end{bmatrix} - \text{O}_{\text{vac}}$$

Along with this majority structure, we also observe arrays of defects with rotations of 120° and 240° with respect to the above orientation on both the larger- and smaller-sized islands on the film. The presence of such areas reinforces the view that ceria films formed in this way are quite highly reduced from stoichiometric CeO_2 .

The mobility of defects on ceria is somewhat disputed. Namai et al.¹³ appeared to observe the diffusion of surface oxygen vacancies across the native $\text{CeO}_2(111)$ surface at room temperatures, whereas Esch et al.⁹ did not observe any such diffusion for temperatures below 673 K . This discrepancy was explained by adsorbate-mediated diffusion.^{9,12} In our experiments, we do not observe any movement of single or multiple surface or subsurface oxygen vacancies for the duration of scanning (minutes) at room temperature. There is, however, some

movement of water molecules and other adsorbate species. It is not yet clear whether this motion is due to interaction with the tip or thermal diffusion across the surface. Tip–surface interactions were considerable in our experiments, as evidenced by the streaking present in many images. This large tip–sample interaction also manifests itself in instability while scanning, such that tips are often only capable of atomic resolution imaging for a few hours at most.

4. Summary

We have used scanning tunnelling microscopy to characterize ultrathin films of CeO₂(111) supported on Pt(111). The films were prepared in two ways, by reactive deposition in O₂ and by postoxidation of Pt/Ce surface alloys. Atomically resolved images of films prepared by both methods revealed remarkable similarities to images recorded in previous studies on CeO₂(111) single crystals using NC-AFM and high-temperature STM. Surface oxygen vacancies were imaged both individually as trimers and in linear arrays. Subsurface oxygen vacancies were also detected. Adsorbed water molecules and surface hydroxide trimers were also imaged, again with a similar appearance to that seen on native CeO₂(111). As such, we conclude that ultrathin ceria films supported on Pt(111) make excellent topographic models for the native oxide.

Acknowledgment. We would like to thank Dr. Greg Cabailh for his valuable advice and discussions. This work was funded by the EPSRC (U.K.) and the COST D41 programme.

References and Notes

- (1) Deluga, G. A.; Salge, J.; Schmitt, L. Renewable Hydrogen from Ethanol by Autothermal Reforming. *Science* **2004**, *303*, 993–997.
- (2) Trovarelli, A. *Catalysis by Ceria and Related Materials*; Imperial College Press: London, 2000; Vol 2.
- (3) Bernal, S.; Calvino, J. J.; Cauqui, M. A.; Gatica, J. M.; Larese, C.; Perez Omil, J. A.; Pintado, J. M. Some Recent Results on Metal/Support Interaction Effects in NM/CeO₂ (NM: Noble Metal) Catalysts. *Catal. Today* **1999**, *50*, 175–206.
- (4) Pfau, A.; Schierbaum, K. D. The Electronic Structure of Stoichiometric and Reduced CeO₂ Surfaces: An XPS, UPS and HREELS Study. *Surf. Sci.* **1994**, *321*, 71–80.
- (5) Mullins, D. R.; Overbury, S. H.; Huntley, D. R. Electron Spectroscopy of Single Crystal and Polycrystalline Cerium Oxide Surfaces. *Surf. Sci.* **1998**, *409*, 307–319.
- (6) Fu, Q.; Saltsburg, H.; Flytzani-Stephanopoulos, M. Active Non-metallic Au and Pt Species on Ceria-Based Water–Gas Shift Catalysts. *Science* **2003**, *301*, 935–938.
- (7) Liu, Z.; Jenkins, S.; King, D. Origin and Activity of Oxidized Gold in Water–Gas-Shift Catalysis. *Phys. Rev. Lett.* **2005**, *94*, 196102.
- (8) Zhang, C.; Michaelides, A.; Jenkins, S.; King, D. Anchoring Sites for Initial Au Nucleation on CeO₂(111): O Vacancy versus Ce Vacancy. *J. Phys. Chem. C* **2009**, *113*, 6411–6417.
- (9) Esch, F.; Fabris, S.; Zhou, L.; Montini, T.; Africh, C.; Fornasiero, P.; Comelli, G.; Rosei, R. Electron Localization Determines Defect Formation on Ceria Substrates. *Science* **2005**, *309*, 752–755.
- (10) Norenberg, H.; Briggs, G. Defect Structure of Nonstoichiometric CeO₂(111) Surfaces Studied by Scanning Tunneling Microscopy. *Phys. Rev. Lett.* **1997**, *79*, 4222–4225.
- (11) Gritschneider, S.; Iwasawa, Y.; Reichling, M. Strong Adhesion of Water to CeO₂(111). *Nanotechnology* **2006**, *18*, 044025.
- (12) Gritschneider, S.; Reichling, M. Structural Elements of CeO₂(111) Surfaces. *Nanotechnology* **2007**, *18*, 044024.
- (13) Namai, Y.; Fukui, K.; Iwasawa, Y. Atom-resolved Noncontact Atomic Force Microscopic Observations of CeO₂(111) Surfaces with Different Oxidation States: Surface Structure and Behavior of Surface Oxygen Atoms. *J. Phys. Chem. B* **2003**, *107*, 11666–11673.
- (14) Torbrügge, S.; Reichling, M.; Ishiyama, A.; Morita, S.; Custance, O. Evidence of Subsurface Oxygen Vacancy Ordering on Reduced CeO₂(111). *Phys. Rev. Lett.* **2007**, *99*, 056101.
- (15) Freund, H. J. Oxide Surfaces. *Faraday Discuss.* **1999**, *114*, 1–31.
- (16) Lu, J.; Gao, H. J.; Shaikhutdinov, S.; Freund, H. J. Morphology and Defect Structure of the CeO₂(111) Films Grown on Ru(0001) as Studied by Scanning Tunneling Microscopy. *Surf. Sci.* **2006**, *600*, 5004–5010.
- (17) Mullins, D.; Radulovic, P.; Overbury, S. Ordered Cerium Oxide Thin Films Grown on Ru(0001) and Ni(111). *Surf. Sci.* **1999**, *429*, 186–198.
- (18) Alexandrou, M.; Nix, R. The Growth, Structure and Stability of Ceria Overlayers on Pd(111). *Surf. Sci.* **1994**, *321*, 47–57.
- (19) Eck, S.; Castellarin-Cudia, C.; Surnev, S.; Ramsey, M. G.; Netzer, F. P. Growth and Thermal Properties of Ultrathin Cerium Oxide Layers on Rh (111). *Surf. Sci.* **2002**, *530*, 173–185.
- (20) Wilson, E. L.; Brown, W.; Thornton, G. CO Adsorption on the Model Catalyst Pd/CeO_{2-x}(111)/Rh(111). *J. Phys. Chem. C* **2007**, *111*, 14215–14222.
- (21) Xiao, W.; Guo, Q.; Wang, E. G. Transformation of CeO₂(111) to Ce₂O₃(0001) Films. *Chem. Phys. Lett.* **2003**, *368*, 527–531.
- (22) Matolin, V.; Libra, J.; Matolinova, I.; Nehasil, V.; Sedlacek, L.; Sutara, F. Growth of Ultra-Thin Cerium Oxide Layers on Cu(111). *Appl. Surf. Sci.* **2007**, *254*, 153–155.
- (23) Desikusumastuti, A.; Staudt, T.; Happel, M.; Laurin, M.; Libuda, J. A Route to Continuous Ultra-Thin Cerium Oxide Films on Cu(111). *Surf. Sci.* **2009**, *603*, 3382–3388.
- (24) Berner, U.; Schierbaum, K. D. Cerium Oxides and Cerium–Platinum Surface Alloys on Pt(111) Single-Crystal Surfaces Studied by Scanning Tunneling Microscopy. *Phys. Rev. B* **2002**, *65*, 10.
- (25) Wilson, E. L.; Grau-Crespo, R.; Pang, C. L.; Cabailh, G.; Chen, Q.; Purton, J. A.; Catlow, C. R. A.; Brown, W. A.; de Leeuw, N. H.; Thornton, G. Redox Behavior of the Model Catalyst Pd/CeO_{2-x}/Pt(111). *J. Phys. Chem. C* **2008**, *112*, 10918–10922.
- (26) Baddeley, C.; Stephenson, A. W.; Hardacre, C.; Tikhov, M.; Lambert, R. M. Structural and Electronic Properties of Ce Overlayers and Low-Dimensional Pt–Ce Alloys on Pt(111). *Phys. Rev. B* **1997**, *56*, 12589–12598.
- (27) Essen, J.; Becker, C.; Wandelt, K. Pt_xCe_{1-x} Surface Alloys on Pt(111): Structure and Adsorption. *e-J. Surf. Sci. Nanotechnol.* **2009**, *7*, 421–428.
- (28) Conesa, J. C. Computer Modeling of Surfaces and Defects on Cerium Dioxide. *Surf. Sci.* **1995**, *339*, 337–352.
- (29) Schierbaum, K. D. Ordered Ultra-Thin Cerium Oxide Overlayers on Pt(111) Single Crystal Surfaces Studied by LEED and XPS. *Surf. Sci.* **1998**, *399*, 29–38.
- (30) Castellarin-Cudia, C.; Surnev, S.; Schneider, G.; Podlucky, R.; Ramsey, M. G.; Netzer, F. P. Strain-Induced Formation of Arrays of Catalytically Active Sites at the Metal–Oxide Interface. *Surf. Sci.* **2004**, *554*, 120–126.

JP102895K